Medical Engineering & Physics 32 (2010) 174–188

Contents lists available at ScienceDirect

Medical Engineering & Physics

journal homepage: www.elsevier.com/locate/medengphy

Cardiac flow component analysis☆

Kelvin K.L. Wong[a,b,*], Jiyuan Tu[a], Richard M. Kelso[c], Stephen G. Worthley[d], Prashanthan Sanders[d], Jagannath Mazumdar[b], Derek Abbott[b]

[a] School of Aerospace, Mechanical & Manufacturing Engineering, RMIT University, PO Box 71, Bundoora, VIC 3083, Australia
[b] Center for Biomedical Engineering and School of Electrical & Electronics Engineering, University of Adelaide, SA 5005, Australia
[c] School of Mechanical Engineering, University of Adelaide, SA 5005, Australia
[d] School of Medicine, University of Adelaide, and Department of Cardiology, Royal Adelaide Hospital, SA 5005, Australia

ARTICLE INFO

Article history:
Received 26 February 2009
Received in revised form
19 November 2009
Accepted 22 November 2009

Keywords:
Component flow analysis
Vorticity
Circulation
Phase contrast magnetic resonance imaging
Segmentation
Data clustering

ABSTRACT

In a chamber of the heart, large-scale vortices are shown to exist as the result of the dynamic blood flow and unique morphological changes of the chamber wall. As the cardiovascular flow varies over a cardiac cycle, there is a need for a robust quantification method to analyze its vorticity and circulation. We attempt to measure vortex characteristics by means of two-dimensional vorticity maps and vortex circulation. First, we develop vortex component analysis by segmenting the vortices using an data clustering algorithm before histograms of their vorticity distribution are generated. The next stage is to generate the statistics of the vorticity maps for each phase of the cardiac cycle to allow analysis of the flow. This is followed by evaluating the circulation of each segmented vortex. The proposed approach is dedicated to examining vortices within the human heart chamber. The vorticity field can indicate the strength and number of large-scale vortices in the chamber. We provide the results of the flow analysis after vorticity map segmentation and the statistical properties that characterize the vorticity components. The success of the cardiac measurement and analysis is illustrated by a case study of the right atrium. Our investigation shows that it is possible to utilize a data clustering algorithm to segment vortices after vorticity mapping, and that the vorticity and circulation analysis of a chamber vorticity can provide new insights into the blood flow within the cardiovascular structure.

1. Introduction

The objective of our study is to develop a flow measurement tool and to test it for effectiveness in analyzing the swirling of blood in the cardiovascular system. With an appropriate scan section, at least one vortex can be observed in a heart chamber such as the right and left atria [1–3], the left ventricle [4–7] or through heart valves [8,5]. Vortices also appear in other components of the blood circulatory system such as the aorta [9,10], the fermoral artery [11], carotid bifurcation [12], or a curved artery [13] in general. The use of magnetic resonance velocity mapping and cardiac imaging enables a good assessment of vortices that exist in the cardiovascular structures [9,14,15,4]. This imaging modality can produce cine-MR images and it is a non-invasive imaging technique that allows study of flow-related physiology and pathophysiology with good spatial and temporal resolutions [16–18].

Gated-MRI [19–23] can be used in this study for the flow imaging of the cardiac chamber in a normal subject. The initial stage involves performing phase contrast MR imaging of the heart at short axis through the heart. The blood motion can be mapped in two dimensions based on combination of the velocity signal maps pertaining to two directions. From these maps, we can develop planar flow maps of blood flow in the chamber and perform flow analysis using the tools that will be described in this paper.

The relationship of the electrocardiogram (ECG) to the cardiac cycle, such that its cyclic period is labelled based on the scan time frame number of the cardiac MR imaging, can be illustrated in Fig. 1. The pressure waveforms of the heart chambers and aorta are provided to indicate the onset of atrial and ventricular contraction with respect to the scan time frames. The flow properties of blood can be related to each cardiac event [24]. We note that blood flows from the *vena cavae* into the atria and directly through the tricuspid valves into the ventricles. The ventricles are responsible for pumping blood to the lungs and through the aorta to the rest of the body. It also causes the atrioventricular valves to close so as to prevent backflows of blood. These changes in heart chamber sizes affects the

☆ The authors developed and use a medical image processing software named Medflovan to produce the results displayed in this paper. This is a system entirely created using the C++ object-oriented programming platform to provide cardiac flow visualization and analysis. Cardiac flow computation and visualization is performed on a Pentium 4-class processor on a dedicated graphics card with 512 MB of memory.

* Corresponding author at: School of Aerospace, Mechanical & Manufacturing Engineering, RMIT University, PO Box 71, Bundoora, VIC 3083, Australia.
Tel.: +61 03 9925 6164.
E-mail address: k.wong@rmit.edu.au (K.K.L. Wong).

1350-4533/$ – see front matter © 2009 IPEM. Published by Elsevier Ltd. All rights reserved.
doi:10.1016/j.medengphy.2009.11.007

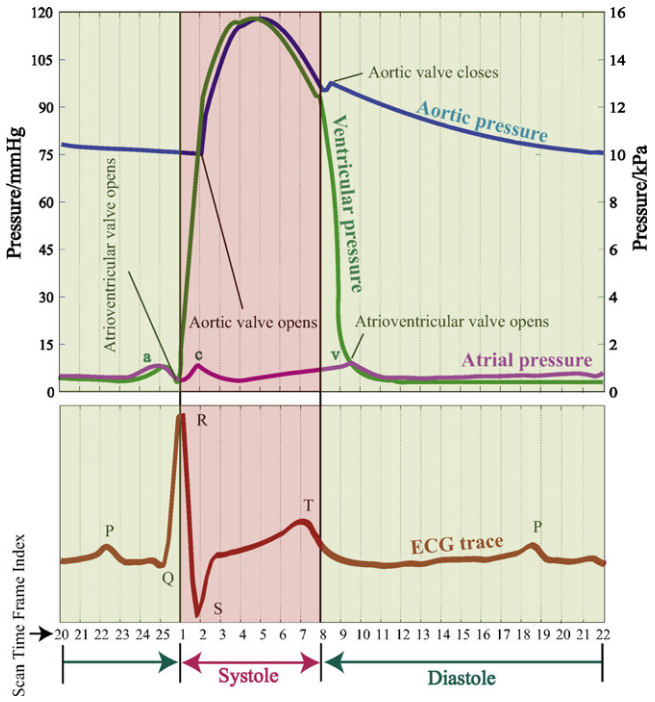

Fig. 1. Cardiac events with relation to scan time frames. The pressure waveforms of the left ventricle, aorta and right atrium is correlated to the scan time frames of gated-MRI. The triggering of image acquisition starts at the occurrence of the R-wave. For a temporal resolution of 25 time frames, the cardiac systole starts from 1 to 8, and the diastole is from 9 to 25. The pressure changes in the atria can be denoted by the minor elevations labelled as *a*, *c*, and *v* waves that are caused by the dynamics of blood during atrial and ventricular contractions.

pressure and the flow patterns of the blood. Therefore, the myocardial movement are intrinsically related to the blood dynamics and we present this diagram depicting the occurrence of the various cardiac events in order to relate the scan time frames with the pressure variations. This helps to provide a preliminary introduction to the cardiovascular dynamics of the heart before we can investigate the flow and to explain our observation and analysis using the appropriate terminologies and with relation to the cardiac event occurrence.

Vorticity within the flow is computed from the velocity field. A segmentation method is utilized to segregate the chamber flow region into areas that contains each large-scale vortex. The number of these vortices can be known by applying an unsupervised data clustering algorithm on the vorticity color map. Then, statistical analysis is executed based on each well-defined vortex. From the data presented in this paper, we have identified two dominant vortices of opposite rotation in the right atrium and presented them for selected time frames of one cardiac cycle. The variation of vorticity mean and circulation for each vortex can be examined during the flow analysis. Information from the statistics of the vortical flow may be able to present flow characteristics and relate to the pressure waveforms of the cardiovascular system.

The purpose of this study is to demonstrate the working principles of our proposed framework that is devised to perform component flow analysis. The mathematical and technical information presented in this paper can lay the fundamentals for further successful flow analysis of any cardiac circulation. Since our objective is not to establish the number of vortices in the heart or to discover new flow phenomenon, but to present an engineering methodology to achieve effective flow analysis, we can justify the testing of this platform using a sample case study of the right atrial flow.

2. Materials and methods

This section describes the concepts of phase contrast magnetic resonance (MR) imaging modalities and a measurement framework to calculate vorticity and quantify this parameter statistically in order to implement a new visualization system for flow patterns in cardiac chambers.

2.1. Phase contrast magnetic resonance imaging velocimetry

As can be observed, phase contrast magnetic resonance imaging encodes velocity information within the output images and we are able to decipher these data to produce velocity field maps for cardiovascular flow [16,25–28]. The magnetic resonance-based framework enables the flow imaging of cardiovascular system non-invasively and with good reliability and without the need for contrast agent to be introduced into the human body. This technology is well established in the medical imaging industry and will be able to serve as a gold standard flow imaging protocol for validation of new methodologies that will be developed.

We present some images based on this magnetic resonance (MR) imaging protocol in Fig. 2. The phase contrast images are graphical representations of the velocity components (x- and y-directions) maps. The figure shows the foot–head (F–H) and anterior–posterior (A–P) orientation scans. Combining the two flow maps based on the in-plane x- and y-directions results in velocity mapping of the blood flow as shown below in Fig. 2.

2.2. Vorticity measurement and statistics of flow map

Vorticity is a quantity that is closely related to the angular velocity of the fluid at a point, and it is evaluated from the fluid velocity gradients [29]. The out-of-plane vorticity component is calculated from the in-plane velocity field using the scheme shown in Fig. 3(a). The circulation is the line integral of the tangential velocity along a circuit (in a counter-clockwise fashion) enclosing a point of interest. The vorticity ω is then equal to the circulation divided by the area enclosed by this circuit.

A pre-requisite to examining the suggested flow parameters is the requirement to develop a finite element differentiation technique for facilitating the computation of velocity field differentiation using data sampled within an interrogation window. Numerical differential operators based on single-level differential operators have been described in various literature [29–33]. We shall examine the approximation of the gradient of a function based on a point of differentiation with reference to a velocity field.

Mathematically, the two-dimensional vorticity may be effectively represented by Wong et al. [3,63] using

$$\omega = \left(\frac{\partial V_y}{\partial x} - \frac{\partial V_x}{\partial y}\right)_{i,j} = \lim_{\Delta x, \Delta y \to 0} \times \frac{1}{N^2} \sum_{m=1}^{N} \sum_{n=1}^{N} \left[\frac{V_y(i+m, j+n) - V_y(i-m, j-n)}{2m\Delta x} - \frac{V_x(i+m, j+n) - V_x(i+m, j-n)}{2n\Delta y}\right]. \quad (1)$$

From the formulation, positive values signify counter-clockwise (CCW) circulation, whereas negative values represent clockwise (CW) rotation of the fluid. Therefore, the magnitudes of these values give an indication of the rate of rotation and its polarity signifies the direction of the rotation. These may be represented by a colour scale with maximum CCW and CW absolute values corresponding to red and blue, respectively.

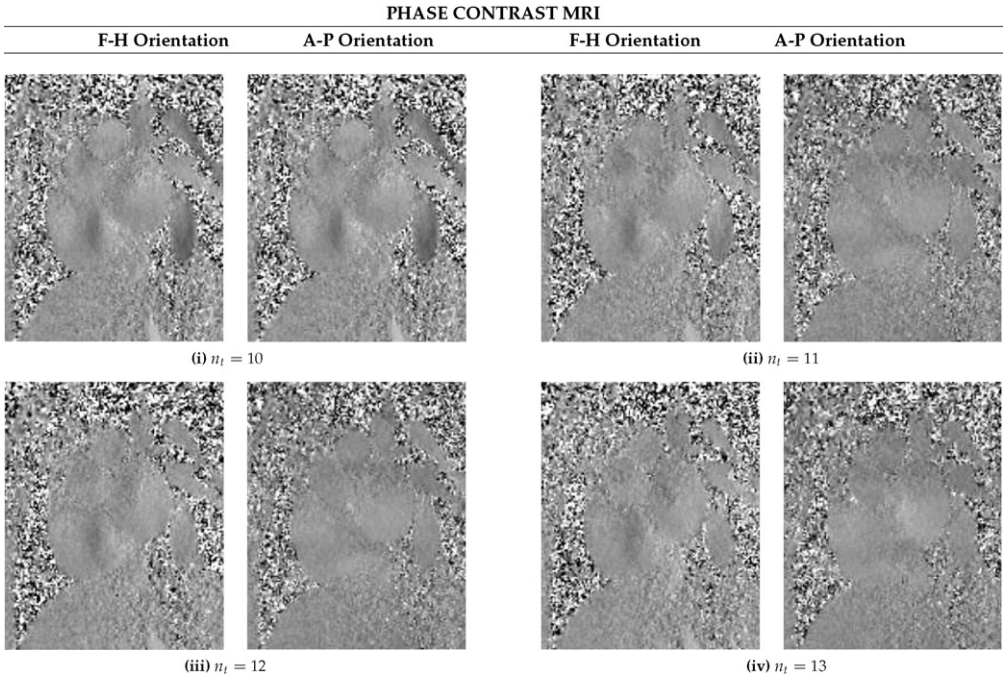

Fig. 2. Phase contrast MRI of a cardiac chamber. Short axis scans pertaining to time frames $n_t = [10, 11, 12, 13]$ out of 25 frames in a cardiac cycle are presented. Scans based on two in-plane *x*- and *y*-directions, which pertains to the foot–head (F–H) and the anterior–posterior (A–P) orientations, respectively, are needed for velocity mapping. The intensity of the pixels in the image indicates the magnitude of the velocity component in the specified orientation. Combining two orthogonal velocity-encoded image maps can produce a two-dimensional velocity flow field.

With these numerical differential methods, $\partial V_y/\partial x$ and $\partial V_x/\partial y$ can be obtained to estimate the vorticity based on the velocity field. From the formulation, positive values signify counter-clockwise (CCW) rotation, whereas negative values represent clockwise (CW) rotation of the fluid.

Next, we perform a statistical analysis of the vorticity distribution. The histogram that is produced, based on the percentage of map area versus the vorticity values $\omega(s^{-1})$ throughout the entire flow map, is featured in Fig. 3(b). A higher resolution of the graph using more horizontal axis intervals results in smaller histogram bar width.

A measure of the average vorticity value is computed by taking the mean $\bar{\omega}_\mu$ or median $\bar{\omega}_m$ of the frequency histograms that are generated from vorticity maps. The magnitudes of these parameters are represented as the blue solid and dash lines, while the centre zero ω line is superimposed onto the frequency graph in grey. The vorticity standard deviations from the flow map measures the relative scatter around the mean and median of the vorticity values in the map, respectively. Standard deviation σ with respect to μ can be computed by considering the variation about the mean, and is denoted as σ_μ. Based on a similar mode of computation, calculating the degree of variation about the median will give σ_m.

It is useful to characterize the amount of swirl by the circulation Γ. Circulation Γ is calculated using the line integral of a closed and counter-clockwise circuit C [34,29]. By using Stokes' theorem, we may write this as a surface integral in Eq. (2) as follows:

$$\oint_c v \cdot dl = \int_s (\nabla \times v) \cdot dS = \int_s \omega \cdot dS. \tag{2}$$

Note that the circulation may be approximated by taking the product of the vorticity mean $\bar{\omega}$ and the area enclosed by the chamber

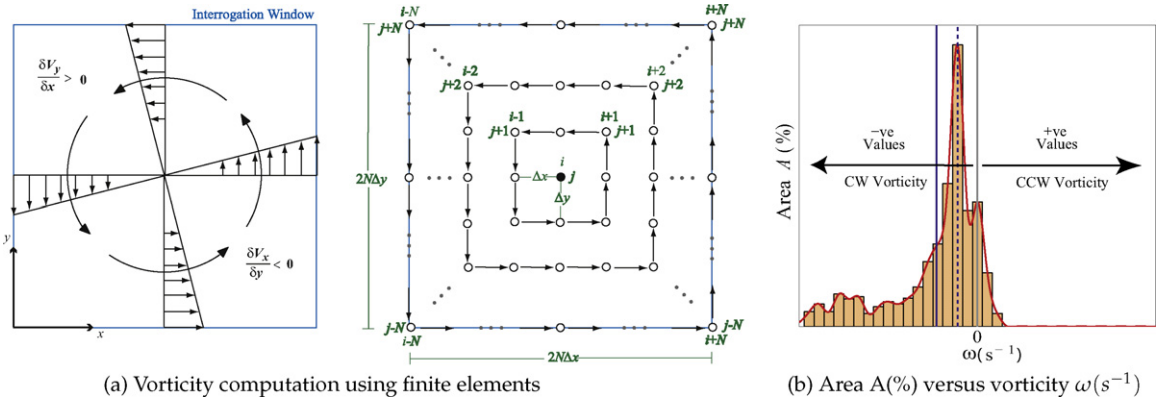

Fig. 3. Vorticity measurement and its histogram representation of the computed map. Display of fluid rotation can be represented using finite elements and flow vectors. Vorticity computation is based on the curl of velocity at a point and numerical calculations is carried out using vectors along contour around a point in the flow field. Histogram depicting the variation of vorticity within the region of analysis gives an indication to the degree of rotation within the fluid. The magnitudes of flow field statistical parameters are represented by superimposing onto the histogram using lines with blue solid and dash formats for the mean and median, respectively. The zero ω line in grey colour represents irrotational flow. (For interpretation of the references to color in this figure legend, the reader is referred to the web version of the article.)

boundary A_c such that

$$\Gamma = \bar{\omega} \times A_c. \quad (3)$$

Here, the meaningful and reliable measure of swirling flow is the circulation and therefore, it becomes important to quantify this parameter along with the vorticity statistics.

2.3. Segmentation of vortices for analysis

This section describes the procedures for vorticity-based segmentation using *K*-means clustering and how analysis can be broken down into examination of individual vortices using histogram plots of the isolated vorticity region. Here, segmentation is the process of partitioning a digital image representing the vorticity field into multiple regions or sets of pixels such that each region represents a large-scale vortex. The goal of segmentation is to change the representation of an image into information that is more meaningful for analysis [35].

2.3.1. Color-based K-means clustering segmentation

Data clustering based on a color image is described here. The pixel classification is based on target colors in the segmentation. The technique of color image segmentation based on *K*-means clustering [36–38] is applied. The number of clusters denoted by *K* affects the color differentiation as a large number of clusters may result in over-segmentation of the image and a small number will not enable sufficient region segregation [39]. The color quantization allows us to differentiate cluster regions which have unique class properties and therefore breaks down the analysis into components.

The algorithm can partition spatial data into *K* clusters [40]. Assume that the feature vectors are denoted by $X = \{x_i | i = 1, 2, \ldots, n\}$. The generalized algorithm initiates *K* cluster centroids *C*, given that $C = \{c_j | j = 1, 2, \ldots, K\}$ and $K < n$, by randomly selecting *K* feature vectors from *X*. The feature vectors are assigned into each group labelled as *j* such that their Euclidean distances to the centroid of the group $G_j = ||x_i - c_j||$ are minimum given that $\forall(x_i, c_j) \epsilon X \times C$. The cluster centroids are computed again based on their group members and the new selection of the feature vectors according to the new cluster centroids is performed. The procedure terminates when there is no change in position of cluster centroids. This algorithm forms the basis of our vortex segmentation whereby the pixels that have intensities that correspond to the vorticity magnitudes in the vorticity map image are clustered into *K* vortex regions.

Other segmentation algorithms exist, such as those that are based on standard statistical methods. One example is the principal component analysis [41], which can provide visualization for a more detailed distribution of the data. This analysis on datasets that consist of major clusters (such as the vortices in our application) allows the principal components to represent the direction near which the major vortices lie.

2.3.2. Segregation of vortices

As an illustration, we ideally position two Lamb–Oseen vortices [42–44] with core centres at a distance of 5 mm apart from each other. The vortices have different directions of rotation. Each vortex is constructed in such as way that we computationally set the flow field to span 10 mm by 10 mm in space, and its maximum velocity magnitude to 10 mm s^{-1}. Note that the velocity field of this flow is represented by a digital image grid with a width of 160 and a height of 240 points matrix size.

From the results describing double vortices in the flow field (Fig. 4(a) and (b)), we are able to visually observe their cores and strength using vorticity flow maps. In addition, from the histogram pertaining to each flow map in Fig. 4(c), we can extract useful statistical properties that reveal some information about the flow field, such as the global directions of the vortices.

We can apply region segmentation of the vorticity map based on the proximity of similar map elements to determine the number of vortices that are present in a flow, and also to produce histogram plots of each distribution cluster (Fig. 4(d)–(i)). We can determine regions with high intra-class and low inter-class similarities [45,46] using a *K*-means algorithm, whereby each set of regional clusters with such a characteristic is given a unique label. Therefore, we can localise vortices within the flow and provide a measure of discriminant measure based on the mean $\bar{\omega}$ and variance σ^2 of the cluster distribution. The discrimination of spatial separation for *N* number of vortices is given by

$$D = \frac{1}{N} \sum_{k=1}^{N} \frac{|\bar{\omega}_k|}{\sigma_k^2}. \quad (4)$$

If *D* is large, it means that the vortices are defined with good intra-class similarities and inter-class dissimilarities. Fig. 4 shows the results of applying segmentation on a pair of idealised Lamb–Oseen vortices and examination of each segmented region using histogram plot of its vorticity distribution. Each homogeneous group of vorticity values is a representation of a vortex. An incorrect input for number of clusters into the *K*-means segmentation framework will result in one or more clusters having almost similar vorticity distribution. It is important that an accurate number of large-scale clusters can be automatically determined by a reliable unsupervised clustering algorithm.

The circulation Γ_j of a vortex component *j* can be obtained by taking the product of the component vorticity mean $\bar{\omega}_j$ (from the segmented vorticity region) and the area A_j covered by the vortex cluster *j* such that

$$\Gamma_j = \bar{\omega}_j \times A_{\text{vor}} \quad \text{where} \quad A_{\text{vor}} = \frac{N_j}{N_c} \times A_c. \quad (5)$$

Here, N_j and N_c are the number of pixels that makes up the vortex component and segmented heart chamber respectively. A_c is defined as the actual area of the heart chamber in units of m^2. The measure of swirling flow using Γ is quantified along with the other statistics based on vorticity. The resolution of the vorticity flow map is dependent on that of the velocity field output by the MRI scanner. The reliability of vortex quantification improves as the resolution of the velocity and vorticity fields increases.

3. Experiments

A description of the case subject, the methods of scanning, procedures carried out for investigation of the heart, parameters for flow quantification and data analysis are given in this section. The main objective of these experiments is to perform the cardiac flow analysis using right atrial vorticities and to understand the flow development over a cardiac cycle.

3.1. Subject for case study

In this study, we performed flow imaging on the right atrium of a healthy male subject, aged 22 years, using phase contrast magnetic resonance imaging. The flow information can be used to explain the behaviour of vortices that develop in the chamber of a heart.

The key motivation in this study is to demonstrate the working principles of our implemented velocimetry system for cardiac flow analysis, and therefore it is not necessary to use a huge volume of test data based on multiple scan slices and more than one case subject. The analysis is based on a single heart slice because it is not the aim of this paper to present population study of a cardiac condition

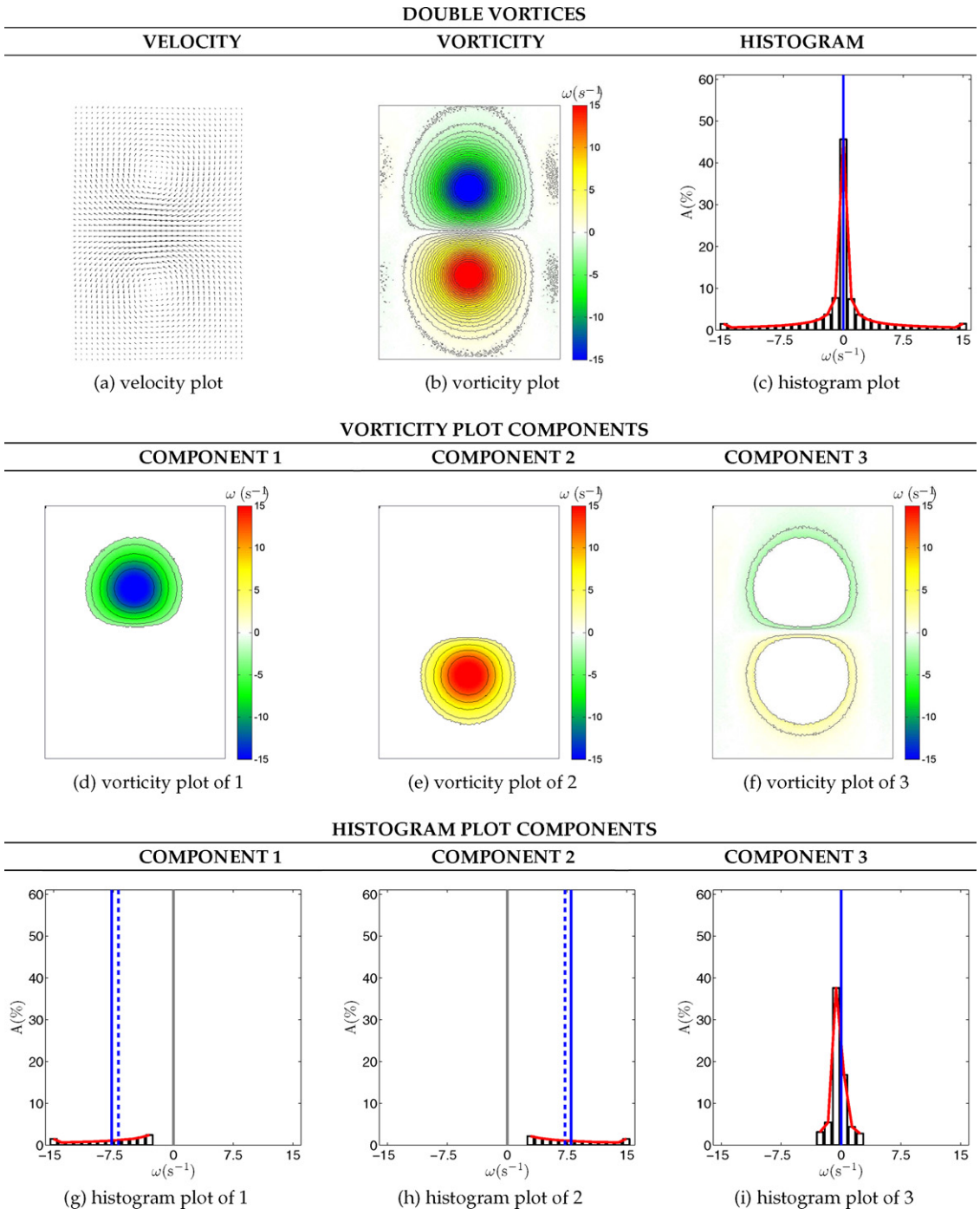

Fig. 4. Localisation and analysis of vortices. Segmentation of flow field isolates the vortices and allows us to perform histogram analysis on its distribution. This enables breakdown of the analysis into components that can be quantified with more quantitative information. In this example, we have two Lamb–Oseen vortices in a flow field and application of *K*-means algorithm segregates the flow region into three partitions. The histogram plot of each partition provides the mean and variance of the isolated vortex which can indicate its vorticity or speed of fluid rotation. Superimposition of the segmented regions results in the combination of their histograms.

in detail. Using a smaller data set will enable use to demonstrate our proposed concepts without increasing the complexity of analysis here.

3.2. MR imaging scan procedure

The velocity-encoded MR imaging was performed using a Siemens Avanto, 1.5 T, model-syngo MRB15 scanner with Numaris-4, Series No: 26406 software. Cine-MR imaging was performed using one slice in short axis views through the atria. All images were acquired with retrospective gating and 25 phases (from $n_t = 1$–25) for a single slice.

Phase contrast magnetic resonance imaging is used to scan the normal subject. Acquisition parameters include: echo time TR = 47.1 ms, repetition time TE = 1.6 ms, field of view FOV = 298 mm × 340 mm at matrix of 134 × 256 pixels. These imaging parameters are chosen for the optimal image acquisition with low signal-to-noise ratio within the atrium. The in-plane and through-

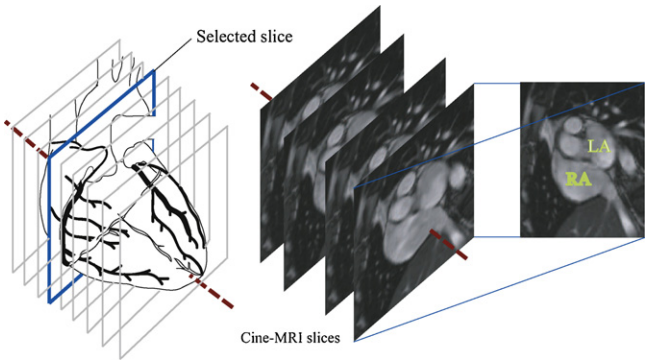

Fig. 5. MR imaging scan through heart of normal subject. The scanning of the heart is taken at short axis and through two chambers, namely the left and right atria. Therefore, this sectional view pertains to the 2-chamber short axis scan. One planar scan is selected for flow examination of the atria.

plane resolution of the scans are determined by the pixel spacing at 1.54 mm/pixel and slice interval of 6 mm, respectively. Velocity encoding (VENC) of 150 cm s^{-1} is applied.

During the scanning, sufficient instructions to the test subject and visual checks were carried out to ensure minimum motion in the scanner. The scanning was performed in such as way that the optimal image resolution can be achieved and with negligible or no motion artifacts. Therefore, there is no need for preprocessing of the image data to correct any significant ghosting artifacts.

3.3. Investigation procedure

Scanning is performed at the section of the heart where the atria are positioned. This section is chosen such that the optimal display of the cross-sectional area of the right atrium is enabled. The scan section is taken at a location shown in Fig. 5 whereby the scan is perpendicular to the axis joining the top of the heart to the apex through the septum. Eleven slices at this orientation are obtained throughout the atria. However, it is effective to base the velocity mapping on the right atrium of the heart using the scan sections that cut though the middle portion of the atria. This corresponds to the largest cross-sectional area of the cardiac chamber. It also enables a better assessment of the vortices as it maximises the number of data points defining each flow feature. One slice as shown in the schematic diagram of the heart is selected for analysis in our study. The full set of images in cine-mode can be viewed using Supplementary Video 1 in Appendix A. Phase contrast MR images for the *x*- and *y*-directions can be viewed using Supplementary Videos 2 and 3 (Appendix A).

4. Results

4.1. Measurements and presentation of right atrial flow

We observe the vortices that appear during the diastolic and systolic phases of the heart beat cycle, and analyze its course of development and changes over the cardiac cycle. The change in polarity of rotation can be easily and visually observed using the streamlines, contour maps, and vector plots as shown in Fig. 6. In addition, we have superimposed the corresponding MR images onto these flow fields to give an indication of the location of the vortex with respect to the chamber that it resides. A vorticity sampling mask of size (21×21) pixel^2 frame is used. This corresponds to 32.34 mm×32.34 mm window size. The rectangular encapsulation of the displayed scan is 184.80 mm×231.00 mm.

We present the flow results and analysis of the right atrium for the selected slice based on one time frame of the cardiac cycle to illustrate the concept of vortex component analysis using real atrial flow data. Using vorticity maps that can be statistically analyzed, histograms are computed based on the vorticity distribution. Note that the mean and median of the histogram are denoted by $\bar{\omega}_\mu$ and $\bar{\omega}_m$, respectively. Standard deviations with respect to the mean and median are denoted as σ_μ and σ_m, respectively.

Fig. 1 shows the flow pressure waveform with all the time frames defined. This is critical in knowing the stages of the cardiac cycle. We focus on a more thorough examination of the flow using the entire set of time frames in this cardiac cycle. For brevity, we present the flow regions based on a selected series of time frames from $n_t = 8$ to 15 out of 25 frames of a cardiac cycle as an illustration (Fig. 7). The full range of vorticity maps can be assessed using Supplementary Video 4 (Appendix A). The statistical entities for every time frame, mean, median and their standard deviations, are displayed to indicate the global properties of the flow. The velocity vector plots show that there are two vortices in the same flow region for the presented time frames. The intensity of vorticity using $\bar{\omega}_\mu$ and σ_μ gives a good estimation of the swirl structure in the right atrium. Based on our conventions, counter-clockwise and clockwise vorticity are represented in red and blue, respectively, on the contour map. Vortices in the atrium are visually shown to be both clockwise and counter-clockwise in rotation upon investigation. This observation needs to be quantified. In Fig. 7, based on $n_t = 8$ to 11, $\bar{\omega}_\mu$ is greater than zero, and the flow is overall counter-clockwise. For $n_t = 12$ to 15, $\bar{\omega}_\mu$ is negative, and the flow becomes clockwise globally. It is reasonable to reach this detection as the sign of $\bar{\omega}_\mu$ is the same as that of Γ.

Next, we performed segmentation on the flow region to segregate the vortices into their components. This can provide a more detailed analysis. In Fig. 8, we present the component analysis for clockwise (CW) and counter-clockwise (CCW) vortices for $n_t = 8$ to 15. The variation of the vortex pattern at every time frame is visible from the intensity contours. The color bar on the right of every vorticity field is scaled to show the actual vorticity range of the segmented vortex.

4.2. Mechanics of flow with reference to the cardiac events

Based on Fig. 1, we attempt to link the flow results to the cardiac events over a heart beat cycle. We highlight the possibility of delay in changes of flow that is caused by the myocardial dynamics at some of these events. This may be due to the time required for the blood to gain momentum. The *v* wave that is caused by right atrial contraction (at time frames $n_t = 23$–1) can cause the pressure to increase up to 6 mmHg [24]. This may account for the rise in vorticity and circulation from $n_t = 23$ to 4. Then, the *c* wave occurs during cardiac systole (from $n_t = 1$ to 8), which causes a slight regurgitation of blood into the atrium at the onset of the ventricular contraction. At this instance, the mitral and tricuspid valves close due to the back pressure of blood flow into the atrium. We can relate this event to the reduction of vorticity and circulation magnitude resulting in decreasing values from $n_t = 5$ to 11. The *v* wave that occurs towards the end of cardiac systole ($n_t = 9$) is the cause of blood flow into the atrium from the *v* ena cavae. This may be observed in the slow increase of vorticity and circulation in the opposite direction (negative values) from $n_t = 12$ to 14. After ventricular contraction, the atrioventricular valves open allowing the stored atrial blood to flow rapidly into the ventricles and causing the *v* wave to disappear ($n_t = 11$). At the same time, it also causes the vorticity and circulation to drop to zero values during $n_t = 15$–18. From this instance to the starting of the next atrial contraction, the two flow properties increases slightly. There should be a marked increase in their values at the onset of the atrial systole ($n_t = 23$).

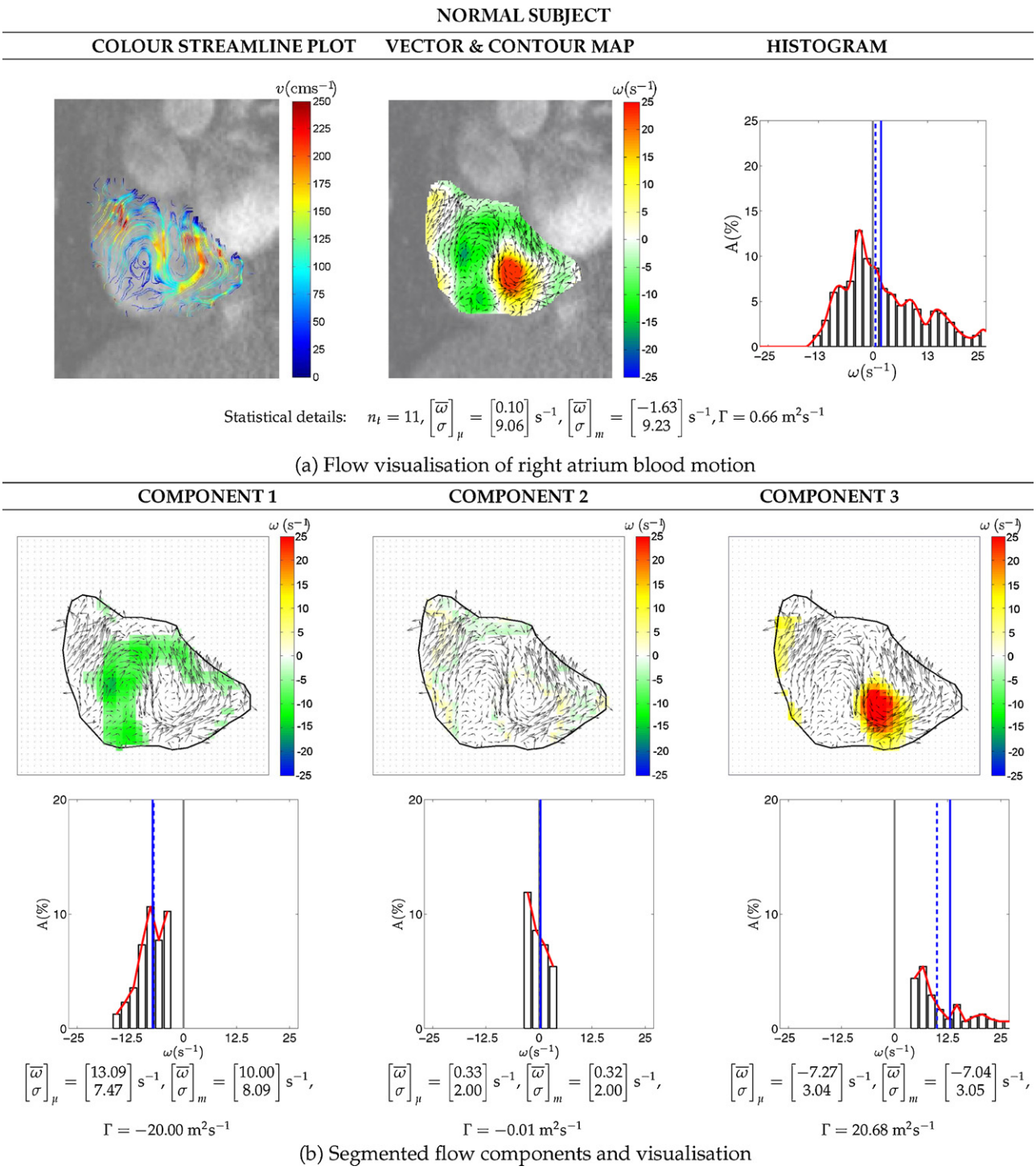

Fig. 6. Component analysis of normal right atrium flow. (a) The visualization of flow in the right atrium of a normal subject is presented for investigation of the vortex behaviour for time frame $n_t = 11$ of one cardiac cycle. The statistical properties are based on the chamber flow region. (b) The segmentation of vortical flow using *K*-means into individual vortices can be performed effectively.

5. Discussion

Flow analysis can be based on the entire flow region and also on individual segregated sub-regions such that each of them comprises of a vortex. A concise analysis of cardiac flow in a heart chamber may be based on the statistical properties of the regional vorticity field. We highlight the systolic phases from approximately $n_t = 1$ to 8 and the diastolic phases from $n_t = 9$ to 25.

5.1. Global flow analysis

For the selected set of time frames based on one cardiac cycle, two vortices are seen to exist in the chamber simultaneously. From Fig. 6, based on the streamline plots and vorticity contour maps, we are able to deduce that one counter-clockwise (CCW) vortex in the atrium exists along with a second clockwise (CW) vortex approximately to the upper-left of it.

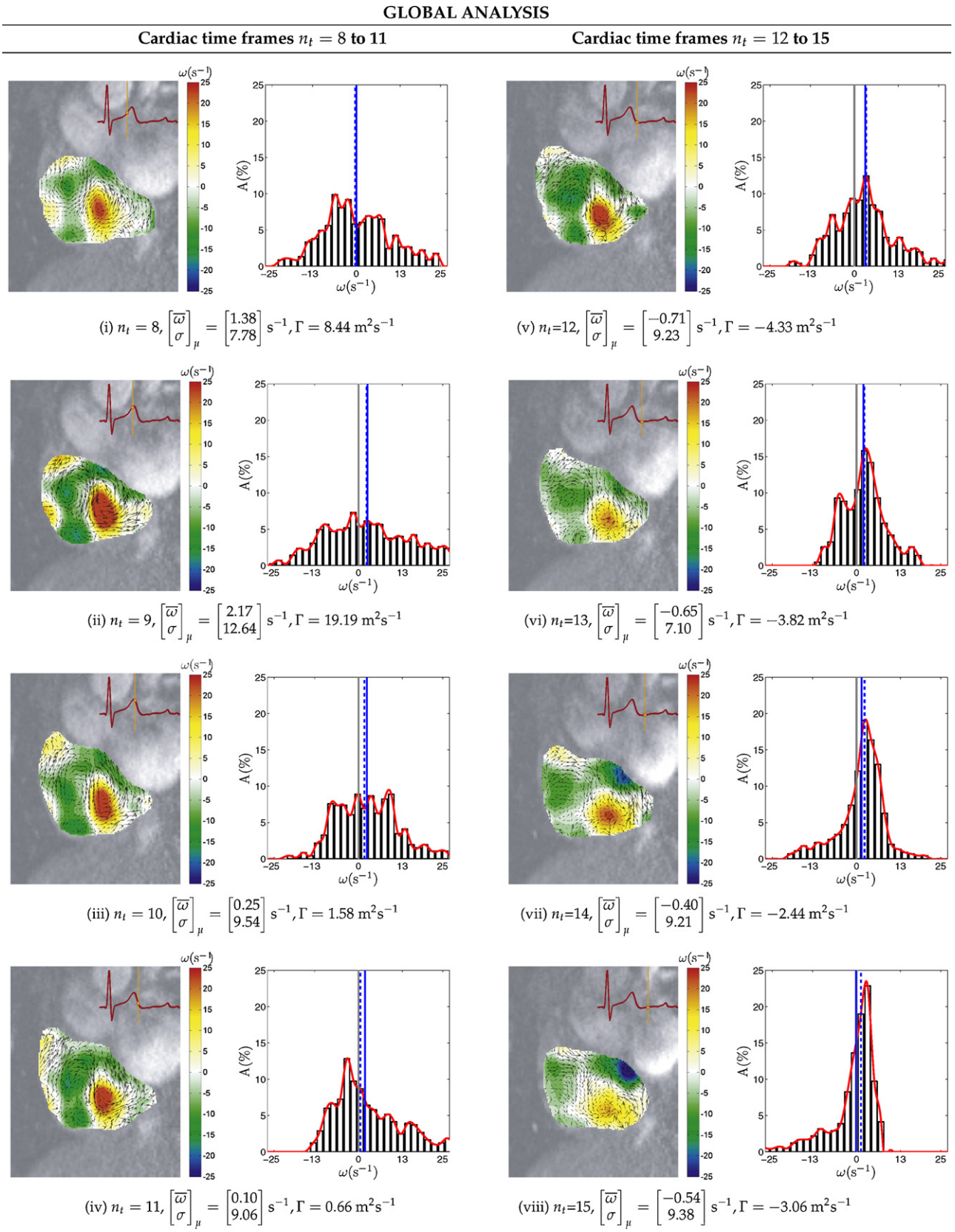

Fig. 7. Global analysis for normal right atrium flow. The visualization of flow in the right atrium of a normal subject is presented based on time frames $n_t = 8$ to 15 out of one cardiac cycle of 25 time phases. The change in flow patterns can be visually analyzed with support of statistical parameters of mean $\bar{\omega}_\mu$, median $\bar{\omega}_m$ and their respective standard deviations σ_μ and σ_m.

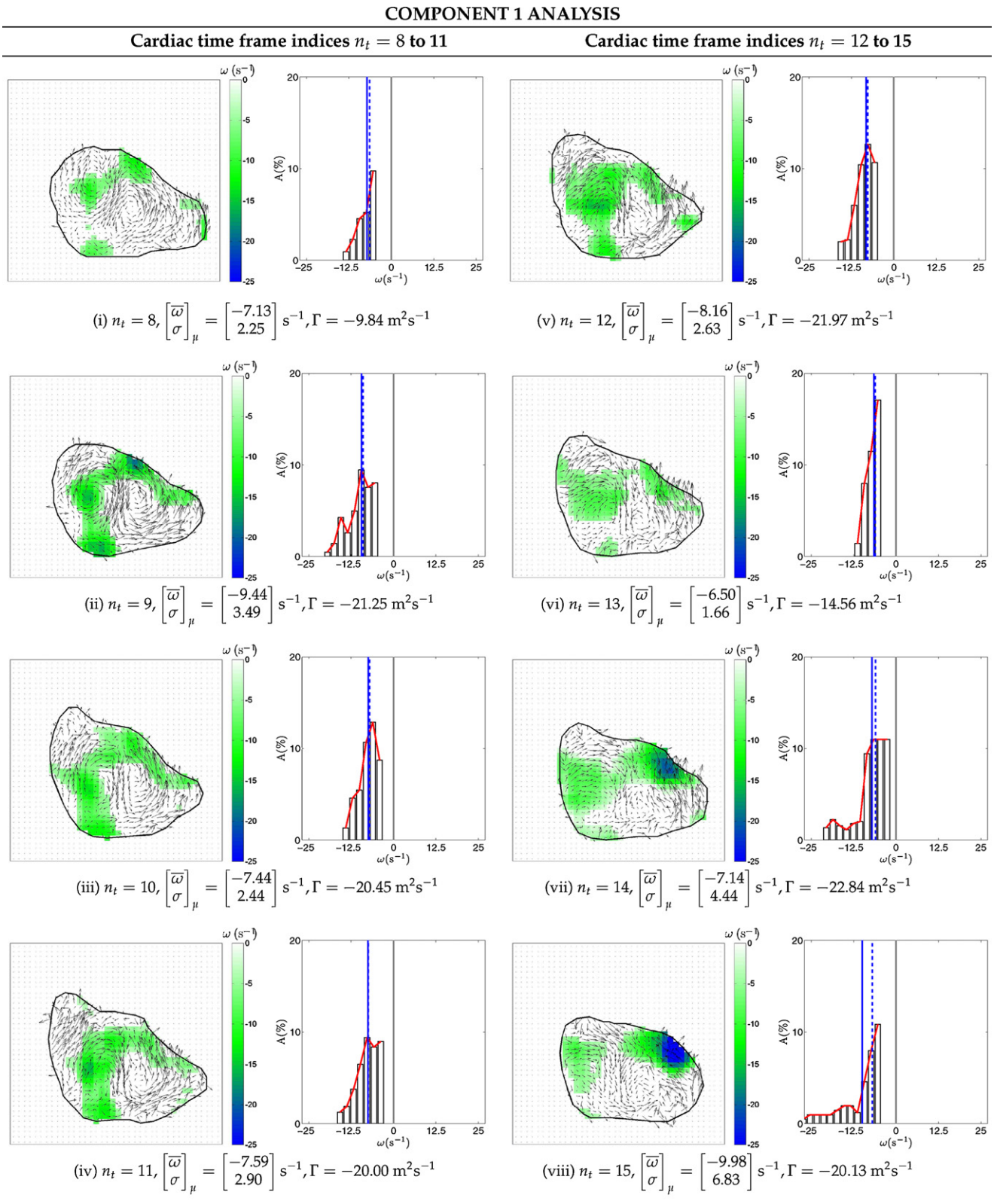

Fig. 8. Component analysis for normal right atrium flow. The visualization of flow in the right atrium of a normal subject is presented based on clockwise (CW) and counter-clockwise (CCW) vortices for analysis of vortex component 1 and 3, respectively. Time frames $n_t = 8$–15 out of one cardiac cycle of 25 time phases are selected for illustration.

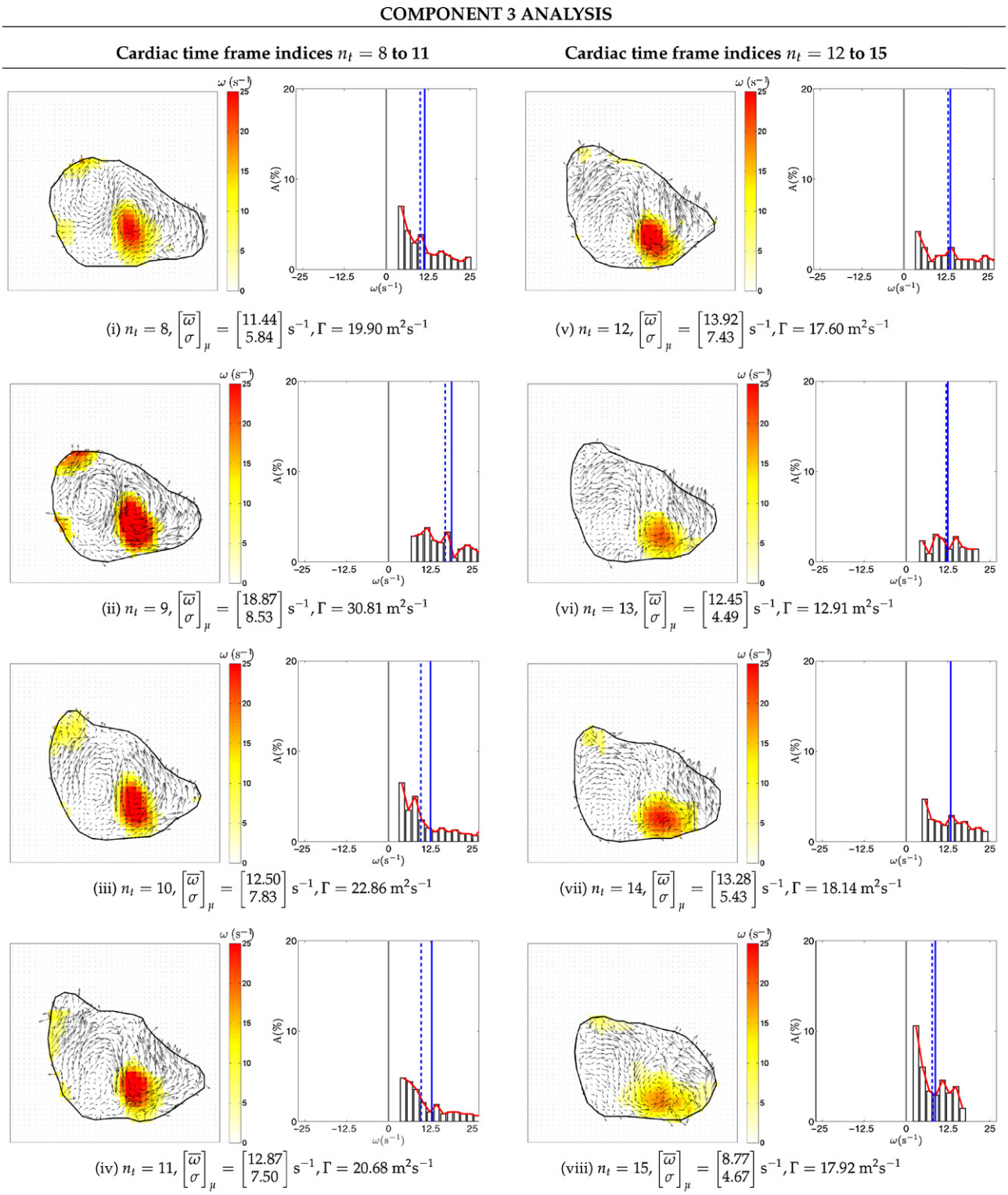

(b) Component analysis for counter-clockwise vortex

Fig. 8. (*Continued*).

Vortical flow based on the contour flow maps for the eight selected times frames of a cardiac cycle is characterised using the "centroid" of the vorticity distribution which can be the mean or median of all the map values. With reference to this case, the mean of the vorticity distribution $\bar{\omega}_\mu$ ranges from -0.66 to $2.13\,s^{-1}$ while its median $\bar{\omega}_m$ ranges from -3.05 to $0.00\,s^{-1}$. Because of higher positive vorticity values generated by a stronger counter-clockwise vortex versus a weaker clockwise vortex, the distribution centroid is offset from the zero value.

Another characteristic of the flow is the variance of the vorticity values, which can be based on its mean or median as the distribution centroid. The standard deviation of vorticity map σ that is based on the mean and median ranges from 7.13 to $12.64\,s^{-1}$ and 7.53 to $12.81\,s^{-1}$, respectively. Vorticity images with high

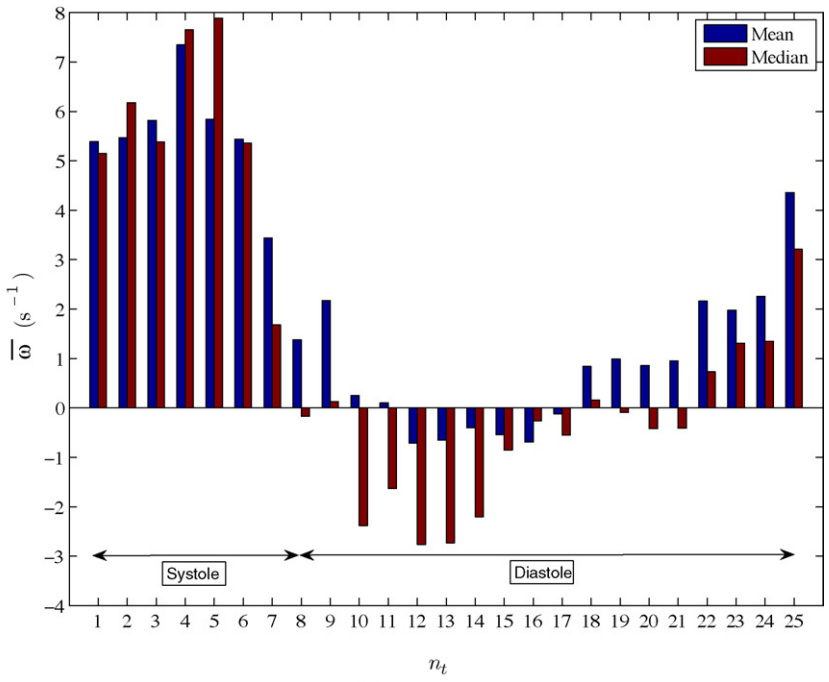

(a) Vorticity mean

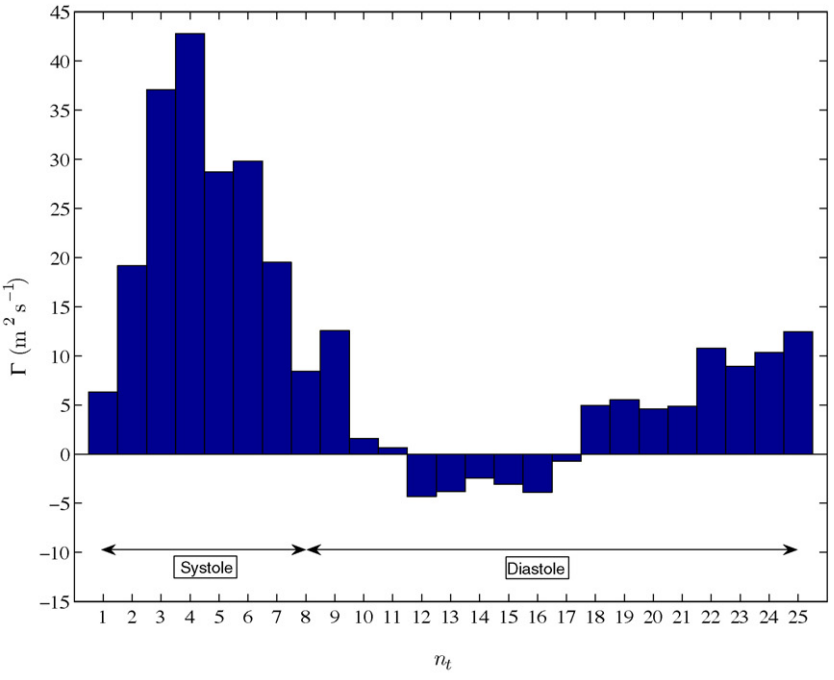

(b) Circulation

Fig. 9. Variation of global vorticity mean and circulation. The variation of (a) vorticity mean $\bar{\omega}$ and (b) circulation for a cardiac cycle of 25 time frames shows that both positive and negative average map values can exist as the result of having two vortices in the flow. The sign of the average map value can indicate the dominance of positive vorticities over the other negative ones.

pixel color contrast result from maps with large standard deviations. There are a few reasons for a high σ, so it is of little value to use it for flow interpretation. Some possible reasons can be the presence of an odd number of equally strong vortices in the flow or numerous small vortices of different strengths, and the new vorticity that may be generated near the chamber wall regions.

The vorticity and circulation charts in Fig. 9 are able to provide evidence of the physical flow occurence that is related to the cardiac events. It can be observed that the vorticity and circulation properties of flow are generally higher and positive (overall clockwise rotation) during the systole and at the transition stage to diastole, the values decreases to zero. For the diastolic events, the flow properties reduces to negative magnitudes (overall counter-clockwise rotation) and slowly increases in value towards the end of the diastole. This section provides an indication of the overall direction of flow circulation. Further analysis can be achieved by analyzing each segmented vortex individually.

5.2. Component flow analysis

Breaking down the vorticity analysis into examination of individual vortices allows us to characterize the blood flow behaviour more accurately. Two main vortices are identified: one of clockwise motion with $\bar{\omega}_\mu$ with range from -14.85 to $-2.42\,s^{-1}$ and $\bar{\omega}_m$ with range -14.29 to $-3.20\,s^{-1}$, while the other vortex has $\bar{\omega}_\mu$ with range 5.59 to $18.87\,s^{-1}$ and $\bar{\omega}_m$ with range 5.33 to $16.89\,s^{-1}$. Based on the mean of vorticity distribution, the standard deviation σ_μ of the negative and positive vorticities ranges from 0.91 to $8.02\,s^{-1}$, and 2.61 to $8.53\,s^{-1}$, respectively. Standard deviation σ_m of the positive and negative vorticities are of range 0.93 to $8.48\,s^{-1}$ and 2.61 to $8.76\,s^{-1}$ respectively. The region of irrotational flow has a low mean of range -1.64 to $1.57\,s^{-1}$ and small standard deviation of range 1.20 to $4.94\,s^{-1}$.

If we combined the vortices in the flow, the ensembled averaging of the positive and negative vorticities result in a mean of range -0.71 to $7.35\,s^{-1}$ and standard deviation of range 4.87 to $12.64\,s^{-1}$. The larger variance in vorticity shows that the global flow differs from those of the components. This will not give a correct insight

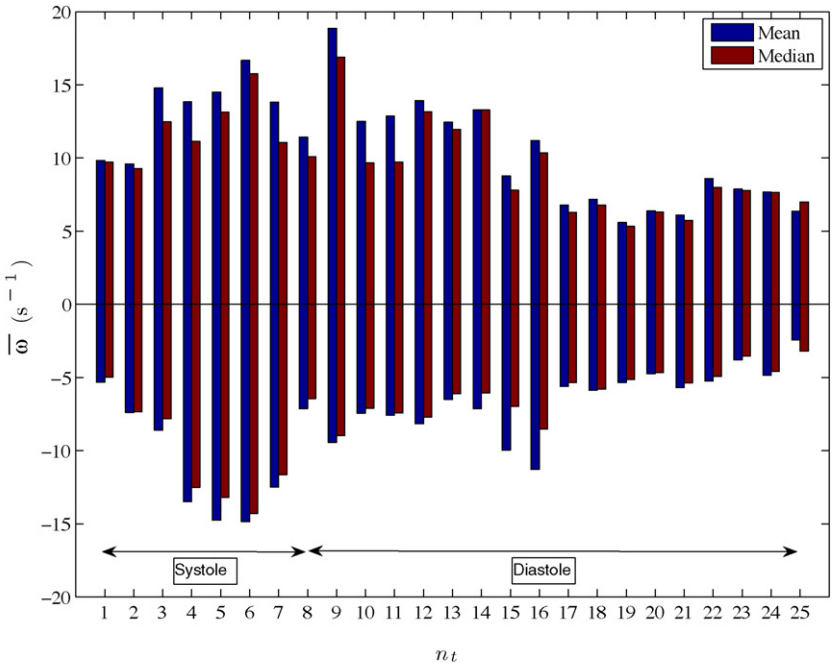

(a)Vorticity mean

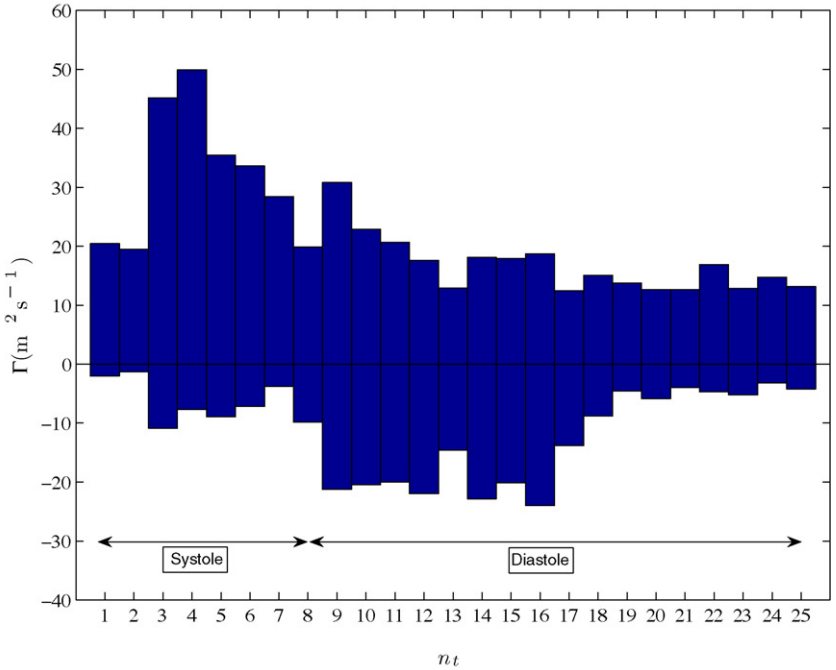

(b)Circulation

Fig. 10. Variation of vorticity mean and circulation of vortex components. The variation of (a) vorticity mean $\bar{\omega}$ and (b) circulation for clockwise and counter-clockwise vorticities are presented by their values at the negative and positive domains of the bar chart, respectively. Note the relatively smaller difference between mean and median values in contrast to those presented in the variation of the statistical properties that pertain to global vorticity.

into the actual flow characteristics. Therefore, we can deduce that vorticity segmentation is crucial for an accurate flow analysis of the blood motion behaviour in the heart.

We have found that, based on normal conditions, two vortices appear during the cardiac cycle (Fig. 10). However, one dominant vortex exists at some time frames. In particular, the presence of a stronger counter-clockwise vortex from $n_t = 1$ to 9 and $n_t = 18$ to 25 can be noted. The clockwise vortex is more dominant from $n_t = 12$ to 16. This is consistent with the global vorticity means presented by Fig. 9. There is a smaller difference between the vorticity mean and median for each time frame, and this is expected because of the smaller standard deviation of vorticity distribution after breaking down the flow regions into their vortex components.

In terms of the temporal variation of flow circulation, the range of Γ for global flow is given by -4.33 to $42.81\,m^2\,s^{-1}$. The counter-clockwise and clockwise vortices have circulation ranges of -24.00 to $-1.30\,m^2\,s^{-1}$ and 12.46 to $49.92\,m^2\,s^{-1}$, respectively. Based on Fig. 10, we may not be able to see much difference in absolute magnitudes between the vorticity means of the clockwise and counter-clockwise vortices. However, the circulation magnitudes of these two vortices are clearly distinguishable during the systole and diastole of the cardiac cycle.

5.3. Overcoming of phase contrast MRI limitations

Estimation of the averaged phases in a voxel is performed considering its asymmetrical distribution about a true average phase. The deviation from the true velocity usually comes from bidirectional flow in the cardiac chamber more than an arterial flow that has a larger unidirectional flow component. However, this may be avoided by setting a higher encoding velocity (VENC) to decrease the signal-to-noise ratio in the phase contrast image [47].

Matching of the VENC becomes a main consideration of the accurate quantification of flow. For VENC that are much larger than the peak velocities, random phases of error or noise becomes prominent. Noise in the phase contrast magnetic resonance images increases with VENC values that are larger than the signal intensities that are registered onto the magnitude images [48]. The noise usually affects the peak velocities and has less influence on the flow estimation as it is averaged over a number of voxels. On the other hand, for VENC that are lower than the peak velocity, aliasing occurs, which results in inverted signal intensities on the images. The suggested method to determine the optimal VENC without aliasing is to start a measurement with a lower VENC and then based on visual judgement, the VENC is modified each step at a time until no aliasing occurs. Such a procedure results in a VENC of $150\,cm\,s^{-1}$ for our case study of the atrial flow. Often with magnetic resonance imaging, there is a limit in the spatial resolution that can be achieved by the scanner, and therefore, flow measurements with a poor spatial resolution may be unable to depict the rotational flow adequately for accurate vorticity mapping. The imaging plane of the heart is appropriate at the location where the maximum cross-sectional area of the cardiac chamber is achieved in order to register as much flow information as possible. By careful adjustments, we are able to obtain a field of view FOV $= 298 \times 340$ mm at matrix of 134×256 pixels. For our study, phase contrast measurements of turbulent or vortical flow decreases in terms of precision. Therefore, we have reduced this error with a shorter echo time (TE) of 1.6 ms for optimal measurement. We have also minimized the case subject movement as much as possible by repeated scannings with the knowledge that spatial misregistration will affect our measurements.

5.4. Clinical relevance of study

The experimental and flow simulation of normal and pathological physiology can provide quantification of the cardiovascular flow functions [17,15,27,49,50]. Such flow information can be used to grade the cardiac health of a patient [51–54]. This motivates the need for cardiac flow measurement from the clinical point of view. The measurement of vorticity based on the cardiac flow field generated from phase contrast MRI velocimetry can have useful applications in the study of cardiac flow for normal subjects [3]. It can also have clinical use for assessing flows in a heart with physical abnormalities, such as septal defects, in addition to evaluation by the well-established transthoracic and transesophoegal echocardiographic techniques [55–62]. By characterising flow using these parameters, and statistically presenting them for every phase of the flow, we are able to extract more information from the flow model. Flow quantification needs to be carried out so that it can have research value and clinical usage. Note that no detailed and quantifiable flow analysis has ever been adequately documented from cardiac blood flow field for diagnostic usage. Even though it may be desirable to analyze the flow quantitatively using planar measurements, it will be inaccurate because the actual flow is three-dimensional. However, we demonstrate that examination and measurement in two-dimensional planes is sufficient in characterising cardiac abnormalities. Clinical trials will be the subject of a future study to show incremental value in using cardiac MRI flow analysis [63]. Advancements in software support for magnetic resonance imaging technology can pave way for future diagnosis of cardiac defects by means of flow analysis within cardiac chambers.

6. Conclusion

We have applied magnetic resonance imaging on the right atrium of a normal subject. The display of information using histograms of vorticity provides an overview of the swirl and strain patterns present within the blood flow. The description of vortical flow in the right atrium can be concisely presented using velocity and vorticity flow maps. Useful visualization tools such as contour and streamline plots are utilized in this paper. More importantly, we are also able to characterise the vortices using histograms of the flow maps and extracting useful statistical properties from vorticity distributions to describe the rotation.

This study demonstrates the methods of characterising a flow field generated using phase contrast magnetic resonance images using vorticity measurement, vortex component breakdown based on an image-clustering algorithm, and statistical analysis of each vortex component after segmentation. Another flow measure, the circulation of the flow is also computed for analysis, and various charts based on these propertise over time can be produced. The technqiues of flow analysis presented here allows us to identify the strength and number of vortices in a heart chamber and this may allow us to physically interpret the cardiac events during a heart beat cycle.

Previous flow analyses are based on qualitative examination of the blood motion without being able to provide any useful and quantitative data. The developed system described in our paper may be of potential clinical utility for assessing abnormal blood flow, and may be a useful tool for discovering and quantifying flow phenomenon in the heart and arteries.

Acknowledgments

The authors thank the Royal Adelaide Hospital for the supply of magnetic resonance images, and to Payman Molaee for his assistance in scanning the subject used in this research. The financial

support provided by the Australian Research Council (ARC project ID DP09786183) is also gratefully acknowledged.

Appendix A. Supplementary data

Supplementary data associated with this article can be found, in the online version, at doi:10.1016/j.medengphy.2009.11.007.

Conflict of interest

We declare that there is no conflict of interests of any kind (financial or personal relationships with other organizations) during the course of this research.

References

[1] Fyrenius A, Ebbers T, Wigström L, Karlsson M, Wranne B, Bolger AF, et al. Left atrial vortices studied with 3D phase contrast MRI. Clinical Physiology and Functional Imaging 1999;19(3):195.
[2] Fyrenius A, Wigström L, Ebbers T, Karlsson M, Engvall J, Bolger AF. Three dimensional flow in the human left atrium. Heart 2001;86:448–55.
[3] Wong KKL, Kelso RM, Worthley SG, Sanders P, Mazumdar J, Abbott D. Cardiac flow analysis applied to phase contrast magnetic resonance imaging of the heart. Annals of Biomedical Engineering 2009;37(8):1495–515.
[4] Kerwin W, Hertzberg J, Cooke J, Chluda H, Shandas R, Gill E. Vorticity imaging of diastolic cardiac inflow by phase-contrast MRI. In: Proceedings of the 2004 IEEE International Symposium on Biomedical Imaging: From Nano to Macro, vol. 1. 2004. p. 300–3.
[5] Pierrakos O, Vlachos PP. The effect of vortex formation on left ventricular filling and mitral valve efficiency. Journal of Biomechanical Engineering-Transactions of ASME 2006;128(4):527–39.
[6] Hong GR, Pedrizzetti G, Tonti G, Li P, Wei Z, Kim JK, et al. Characterization and quantification of vortex flow in the human left ventricle by contrast echocardiography using vector particle image velocimetry. Journal of American Collage of Cardiological Imaging 2008;1:705–17.
[7] Schenkel T, Malve M, Reik M, Markl M, Jung B, Oertel H. MRI-based CFD analysis of flow in a human left ventricle: methodology and application to a healthy heart. Annals of Biomedical Engineering 2009;37(3):503–15.
[8] Shi Y, Zhao Y, Yeo TJ, Hwang NH. Numerical simulation of opening process in a bileaflet mechanical heart valve under pulsatile flow condition. Journal of Heart Valve Disease 2003;12(2):245–55.
[9] Kilner PJ, Yang GZ, Mohiaddin RH, Firmin DN, Longmore DB. Helical and retrograde secondary flow patterns in the aortic arch studied by three-directional magnetic resonance velocity mapping. Circulation 1993;88:2235–47.
[10] Chandran KB. Flow dynamics in the human aorta. Journal of Biomechanical Engineering 1993;115(4B):611–6.
[11] Wood NB, Zhao SZ, Zambanini A, Jackson M, Gedroyc W, Thom SA, et al. Curvature and tortuosity of the superficial femoral artery: a possible risk factor for peripheral arterial disease. Journal of Applied Physiology 2006;101:1412–8.
[12] Zhao SZ, Papathanasopoulou P, Long Q, Marshall I, Xu XY. Comparative study of magnetic resonance imaging and image-based computational fluid dynamics for quantification of pulsatile flow in a carotid bifurcation phantom. Annals of Biomedical Engineering 2003;31(8):962–71.
[13] Hoogstraten HW, Kootstra JG, Hillen B, Krijger JK, Wensing PJ. Numerical simulation of blood flow in an artery with two successive bends. Journal of Biomechanics 1996;29(8):1075–83.
[14] Kilner PJ. Morphodynamics of flow through the heart. PhD thesis, University of London, 1998.
[15] Kilner PJ, Yang G-Z, Wilkes AJ, Mohiaddin RH, Firmin DN, Yacoub MH. Asymmetric redirection of flow through the heart. Nature Medicine 2000;404:759–61.
[16] Wigstrom L, Sjoqvist L, Wranne B. Temporally resolved 3D phase contrast imaging. Magnetic Resonance In Medicine 1996;36:800–3.
[17] Powell AJ, Maier SE, Chung T, Geva T. Phase-velocity cine magnetic resonance imaging measurement of pulsatile blood flow in children and young adults: in vitro and in vivo validation. Pediatric Cardiology 2000;21:104–10.
[18] Dall'Armellina E, Hamilton CA, Hundley WG. Assessment of blood flow and valvular heart disease using phase-contrast cardiovascular magnetic resonance. Echocardiography 2007;24(2):207–16.
[19] Morgan-Hughes GJ, Marshall AJ, Roobottom C. Morphologic assessment of patent ductus arteriosus in adults using retrospectively ECG-gated multidetector CT. American Journal of Roentgenology 2003;181:749–54.
[20] Thompson RB, McVeigh ER. Flow-gated phase-contrast MRI using radial acquisitions. Magnetic Resonance in Medicine 2004;52(3):598–604.
[21] Tetsuya M. ECG gating in cardiac MRI. Japanese Journal of Magnetic Resonance in Medicine 2003;23(4):120–30.
[22] Larson AC, White RD, Laub G, McVeigh ER, Li D, Simonetti OP. Self-gated cardiac cine MRI. Magnetic Resonance in Medicine 2004;51(1):93–102.
[23] Nijm GM, Sahakian AV, Swiryn S, Carr JC, Sheehan JJ, Larson AC. Comparison of self-gated cine MRI retrospective cardiac synchronization algorithms. Journal of Magnetic Resonance Imaging 2008;28(3):767–72.
[24] Guyton AC, Hall JE. Textbook of medical physiology. 11th ed. Elsevier Saunders; 2006.
[25] Markl M, Chan FP, Alley MT, Wedding KL, Draney MT, Elkins CJ, et al. Time-resolved three-dimensional phase-contrast MRI. Journal of Magnetic Resonance Imaging 2003;17:499–506.
[26] Markl M, Draney MT, Hope MD, Levin JM, Chan FP, Alley MT, et al. Time-resolved 3-dimensional velocity mapping in the thoracic aorta: visualization of 3-directional blood flow patterns in healthy volunteers and patients. Journal of Computer Assisted Tomography 2004;28:459–68.
[27] Markl M, Harloff A, Bley TA, Zaitsev M, Jung B, Weigang E, et al. Time-resolved 3D MR velocity mapping at 3T: improved navigator-gated assessment of vascular anatomy and blood flow. Journal of Magnetic Resonance Imaging 2007;25:824–31.
[28] Wong KKL, Kelso RM, Worthley SG, Sanders P, Mazumdar J, Abbott D. Medical imaging and processing methods for cardiac flow reconstruction. Journal of Mechanics in Medicine and Biology 2009;9(1):1–20.
[29] Raffel M, Willert C, Kompenhans J. Particle image velocimetry. Berlin Heidelberg, Germany: Springer-Verlag; 1998.
[30] Fouras A, Soria J. Accuracy of out-of-plane vorticity measurements derived from in-plane velocity field data. Experiments in Fluids 1998;25:409–30.
[31] Foucaut JM, Stanislas M. Some considerations on the accuracy and frequency response of some derivative filters applied to particle image velocimetry vector fields. Measurement Science and Technology 2002;13:1058–71.
[32] Etebari A, Vlachos PP. Improvements on the accuracy of derivative estimation from DPIV velocity measurements. Experiments in Fluids 2005;39(6):1040–50.
[33] Alvarez L, no CAC, García M, Krissian K, Mazorra L, Salgado A, et al. Variational second order flow estimation for PIV sequences. Experiments in Fluids 2008;44(2):291–304.
[34] Potter MC, Wiggert DC. Mechanics of fluids. 2nd ed. Prentice-Hall International, Inc.; 1997.
[35] Shapiro LG, Stockman GC. Computer vision. New Jersey: Prentice-Hall; 2001, ISBN 0-13-030796-3.
[36] Lucchese L, Mitra SK. Unsupervised segmentation of color images based on *k*-means clustering in the chromaticity plane. In: Proceedings of the IEEE Workshop on Content-Based Access of Image and Video Libraries. 1999. p. 74–8.
[37] Kanungo T, Mount DM, Netanyahu NS, Piatko CD, Silverman R, Wu AY. An efficient *k*-means clustering algorithm: analysis and implementation. IEEE Transactions on Pattern Analysis and Machine Intelligence 2002;24(7):881–92.
[38] Ilea DE, Whelan PF. Color image segmentation using a spatial *k*-means clustering algorithm, IMVIP 2006-10th International Machine Vision and Image Processing Conference.
[39] Hase H, Yoneda M, Tokai S, Kato J, Suen CY. Color segmentation for text extraction. International Journal on Document Analysis and Recognition 2003;6(4):271–84.
[40] Wu M-N, Lin C-C, Chang C-C. Brain tumor detection using color-based K-means clustering segmentation. In: Proceedings of the Third International Conference on Intelligent Information Hiding and Multimedia Signal Processing, vol. 2. 2007. p. 245–50.
[41] Jolliffe IT. Principal Component Analysis, Series: Springer Series in Statistics. 2 edn NY, USA: Springer; 2002, ISBN 978-0-387-95442-4.
[42] Saffman P. Vortex dynamics. 1st ed. Cambridge University Press; 1992.
[43] Meunier P, Dizes SL, Leweke T. Physics of vortex merging. Comptes Rendus Physique 2005;6(4-5):431–50.
[44] Cariteau B, Flór JB. An experimental investigation on elliptical instability of a strongly asymmetric vortex pair in a stable density stratification. Nonlinear Processes in Geophysics 2006;13(6):641–9.
[45] Kaufman L, Rousseeuw P. Finding groups in data: an introduction to cluster analysis. John Wiley and Sons; 1990.
[46] Biswas G, Weinberg JB, Fisher DH. ITERATE: a conceptual clustering algorithm for data mining. IEEE Transactions on Systems, Man, and Cybernetics, Part C: Applications and Reviews 1998;28(2):219–30.
[47] Hamilton CA, Moran PR, Santago P, Rajala SA. Effects of intravoxel velocity distributions on the accuracy of the phase-mapping method in phase-contrast MR angiography. Journal of Magnetic Resonance Imaging 2005;4(5):752–5.
[48] Lotz J, Meier C, Leppert A, Galanski M. Cardiovascular flow measurement with phase-contrast MR imaging: basic facts and implementation. Radiographics 2002;22:651–71.
[49] Ghista ND, Ng EY-K. Cardiac perfusion and pumping engineering (clinically-oriented biomedical engineering). World Scientific Publishing Company; 2007.
[50] Ghista ND. Applied biomedical engineering mechanics. CRC Press; 2008.
[51] Vasan RS, Larson MG, Benjamin EJ, Evans JC, Reiss CK, Levy D. Congestive heart failure in subjects with normal versus reduced left ventricular ejection fraction. Journal of the American College of Cardiology 1999;33:1948–55.
[52] Zile MR, Brutsaert DL. New concepts in diastolic dysfunction and diastolic heart failure. Part I. Circulation 2002;105:1387–93.
[53] Hasegawa H, Little WC, Ohno M, Brucks S, Morimoto A, Cheng H-J, et al. Diastolic mitral annular velocity during the development of heart failure. Journal of the American College of Cardiology 2003;41:1590–7.
[54] Gharib M, Rambod E, Kheradvar A, Sahn DJ, Dabiri JO. A global index for heart failure based on optimal vortex formation in the left ventricle. Proceedings of the National Academy of Sciences, United States of America 2006;103(16):6305–8.
[55] Hirsch R, Kilner PJ, Connelly MS, Redington MGSJSAN, Somerville J. Diagnosis in adolescents and adults with congenital heart disease. Prospective assessment of individual and combined roles of magnetic resonance imaging and transesophageal echocardiography. Circulation 1994;90:2937–51.

[56] Hoppe UC, Dederichs B, Deutsch HJ, Theissen P, Schicha H, Sechtem U. Congenital heart disease in adults and adolescents: comparative value of transthoracic and transesophageal echocardiography and MR imaging. Radiology 1996;199(3):669–77.
[57] Abdel-Massih T, Dulac Y, Taktak A, Aggoun Y, Massabuau P, Elbaz M, et al. Assessment of atrial septal defect size with 3D-transesophageal echocardiography: comparison with balloon method. Echocardiography 2005;22(2):121–7.
[58] Kasliwal RR, Chouhan NS, Sinha A, Gupta P, Tandon S, Trehan N. Real-time three-dimensional transthoracic echocardiography. Indian Heart Journal 2005;57(2):128–37.
[59] Bartel T, Konorza T, Barbieri V, Erbel R, Pachinger O, Müller S. Single-plane balloon sizing of atrial septal defects with intracardiac echocardiography: an advantageous alternative to fluoroscopy. Journal of the American Society of Echocardiography 2008;21(6):737–40.
[60] Roldán F-J, Vargas-Barrón J, Vázquez-Antona C, Castellanos LM, Erdmenger-Orellana J, Romero-Cárdenas A, et al. Three-dimensional transesophageal echocardiography of the atrial septal defects. Cardiovascular Ultrasound 2008;6(1):38.
[61] Piatkowski R, Scislo P, Kochanowski J, Transoesophageal real-time three-dimensional echocardiography in assessing large multiperforated atrial septal aneurysm, European Heart Journal 2009;30:1153.
[62] Skolnick A, Vavas E, Kronzon I. Optimization of ASD assessment using real time three-dimensional transesophageal echocardiography. Echocardiography 2009;26(2):233–5.
[63] Wong KKL, Kelso RM, Worthley SG, Sanders P, Mazumdar J, Abbott D. Non-invasive cardiac flow assessment using high speed magnetic resonance fluid motion tracking. PLoS One 2009;4(5):e5688.